

# Nanoscale Imaging of High-Field Magnetic Hysteresis in Meteoritic Metal Using X-Ray Holography

Roberts Blukis<sup>1</sup>, Bastian Pfau<sup>2</sup>, Christian Günther<sup>3</sup>, Piet Hessing<sup>2</sup>, Stefan Eisebitt<sup>2</sup>, Joshua Franz Einsle<sup>4</sup>, and Richard Harrison<sup>5</sup>

<sup>1</sup>GFZ German Research Centre for Geosciences

<sup>2</sup>Max-Born-Institut

<sup>3</sup>Technische Universität Berlin

<sup>4</sup>School of Geographical and Earth Sciences

<sup>5</sup>University of Cambridge

November 26, 2022

## Abstract

Stable paleomagnetic information in meteoritic metal is carried by the cloudy zone  $\sim$ 1-10 micron wide regions containing islands of ferromagnetic tetrataenite embedded in a paramagnetic antitaenite matrix. Due to their small size and high coercivity ( $\sim$ 2.2 T), the tetrataenite islands carry very stable magnetic remanence. However, these characteristics also make it difficult to image their magnetic state with the necessary spatial resolution and applied magnetic field. Here we describe the first application of X-ray holography to image the magnetic structure of the cloudy zone of the Tazewell III CD meteorite with spatial resolution down to  $\sim$ 40 nm and in applied magnetic fields up to 1.1 T, sufficient to extract high-field hysteresis data from individual islands. Images were acquired as a function of magnetic fields applied both parallel and perpendicular to the surface of a  $\sim$ 100 nm thick slice of the cloudy zone. Broad distributions of coercivity are observed, including values that likely exceed the maximum applied field. Horizontal offsets in the hysteresis loops indicate an interaction field distribution with half width of  $\sim$ 100 mT between the islands in their room-temperature single-domain state, providing a good match to first-order reversal curve diagrams. The role of interactions during the acquisition of transformation chemical remnant magnetization as the meteorite parent body is cooled, and the implications for extracting quantitative estimates of the paleofield, are discussed

## Hosted file

supporting information.docx available at <https://aureoria.com/users/554687/articles/605709-nanoscale-imaging-of-high-field-magnetic-hysteresis-in-meteoritic-metal-using-x-ray-holography>

# Nanoscale Imaging of High-Field Magnetic Hysteresis in Meteoritic Metal Using X-Ray Holography

R. Blukis<sup>1\*</sup>, B. Pfau<sup>2</sup>, C. M. Günther<sup>3</sup>, P. Hensing<sup>2</sup>, S. Eisebitt<sup>2,4</sup>, J. Einsle<sup>5</sup>, R. J. Harrison<sup>6</sup>

<sup>1</sup>GFZ German Centre for Geosciences, Telegrafenberg, 14473 Potsdam, Germany

<sup>2</sup>Max-Born-Institut, Max-Born-Straße 2A, 12489 Berlin, Germany.

<sup>3</sup>Technische Universität Berlin, Center for Electron Microscopy (ZELMI), Straße des 17. Juni 135, 10623 Berlin, Germany

<sup>4</sup>Technische Universität Berlin, Institut für Optik und Atomare Physik, Straße des 17. Juni 135, 10623 Berlin, Germany

<sup>5</sup>School of Geographical and Earth Sciences, University of Glasgow, G12 8QQ, UK

<sup>6</sup>Department of Earth Sciences, University of Cambridge, Downing street, Cambridge, CB2 3EQ, UK

Corresponding author: Roberts Blukis ([roberts.blukis@gfz-potsdam.de](mailto:roberts.blukis@gfz-potsdam.de))

## Key Points:

- X-ray holography enables magnetisation of natural samples to be imaged with ~40 nm resolution and in applied magnetic fields up to  $\pm 1.1$  T.
- Meteoritic cloudy zone consists of strongly interacting single-domain particles with single-particle coercivities up to 1 T.
- Average interaction fields between particles in the cloudy zone are of the order 100-200 mT.

---

1 \*Corresponding author

## Abstract

Stable paleomagnetic information in meteoritic metal is carried by the ‘cloudy zone’: ~1-10  $\mu\text{m}$  wide regions containing islands of ferromagnetic tetrataenite embedded in a paramagnetic antitaenite matrix. Due to their small size and high coercivity (~2.2 T), the tetrataenite islands carry very stable magnetic remanence. However, these characteristics also make it difficult to image their magnetic state with the necessary spatial resolution and applied magnetic field. Here we describe the first application of X-ray holography to image the magnetic structure of the cloudy zone of the Tazewell III CD meteorite with spatial resolution down to ~40 nm and in applied magnetic fields up to  $\pm 1.1$  T, sufficient to extract high-field hysteresis data from individual islands. Images were acquired as a function of magnetic fields applied both parallel and perpendicular to the surface of a ~100 nm thick slice of the cloudy zone. Broad distributions of coercivity are observed, including values that likely exceed the maximum applied field. Horizontal offsets in the hysteresis loops indicate an interaction field distribution with half width of ~100 mT between the islands in their room-temperature single-domain state, providing a good match to first-order reversal curve diagrams. The role of interactions during the acquisition of transformation chemical remnant magnetization as the meteorite parent body is cooled, and the implications for extracting quantitative estimates of the paleofield, are discussed.

## Plain Language Summary

Magnetic fields played a significant role in the formation of the solar system and the evolution of the early planetary bodies in the first few million years after solar system formation. Knowledge about magnetic fields in the early solar system can be obtained from meteorites. Some meteorite types contain abundant iron-nickel alloy that contain nanoscale “cloudy zone” regions (named after their appearance in an optical microscope) that can preserve magnetic information over 4.5 billion years. The cloudy zone is a complex material consisting of highly magnetically stable nanoscale particles embedded in a non-magnetic matrix in very close proximity to one another. The fine scale and extreme magnetic stability of the cloudy zone make it challenging to study using conventional magnetic microscopy techniques. Here we apply X-ray holography for the first time to image the magnetisation of individual magnetic particles and how they respond to magnetic fields. This new approach enables us to measure the magnetic properties of individual nanoscale particles, providing the first direct measurement of their magnetic stability and the strength of particle interactions. These measurements will improve our understanding of the magnetic information carried by the cloudy zone, and how to extract information about solar system magnetic fields.

## 1 Introduction

### 1.1 Magnetic fields in the early Solar system and their extraction

Magnetic fields are thought to have played an important role in driving the inward transport of mass and outward transport of angular momentum during the evolution of the early solar system, and are necessary to account for the high accretion rates of protoplanetary disks observed astronomically (Wardle 2007; Bai and Stone 2013; Simon et al. 2013; Santos et al. 2018). Nebula magnetic fields in our solar system were relatively short lived, shutting down as the nebula gas dissipated ~ 4 Myr after the formation of calcium aluminium inclusions (CAIs)

(Wang et al. 2017). A longer-lived source of magnetic fields in the early solar system comes from differentiated planetesimals, which are thought to have generated magnetic fields driven by thermal and/or chemical convection within their liquid iron cores for 10s or even 100s of Myr after CAI formation. Evidence of both nebular and planetesimal fields is obtained from the meteorite record (Fu et al. 2012, 2014; Bryson et al. 2015). The ability to make quantitative paleomagnetic measurements of past magnetic fields from meteorites is an important tool for constraining astrophysical models of star system formation and the thermal, chemical and physical properties of planetesimals.

Obtaining reliable paleomagnetic data from meteorites is made more difficult by the nature of their magnetic remanence carriers. Many planetesimals formed under highly reducing conditions, meaning that their magnetic mineralogy is dominated by iron-nickel metal (e.g., kamacite, taenite) with very different magnetic properties to the iron oxides (e.g., magnetite, hematite) that are the mainstay of terrestrial paleomagnetic studies. Magnetically soft kamacite (a ferromagnetic iron-nickel alloy with body-centered cubic structure), is common in many meteorites. The poor paleomagnetic recording properties of multi-domain (MD) kamacite lead many researchers to conclude that paleomagnetic measurements of metal-rich meteorites were not possible. New high-spatial-resolution ‘nanopaleomagnetic’ methods, however, have enabled paleomagnetic information to be extracted from meteoritic metal. This approach uses X-ray photoemission electron microscopy (XPEEM) to target magnetic measurements at the ‘cloudy zone’:  $\sim 1\text{-}10\ \mu\text{m}$ -sized sub-regions of the metal that contain abundant single-domain (SD) particles (islands) of tetrataenite, a tetragonal form of ordered FeNi with exceptional magnetic stability. This method has been applied successfully to study meteoritic metal in iron and stony-iron meteorites, yielding paleomagnetic information that is not accessible by other techniques (Bryson et al. 2015, 2017; Nichols et al. 2016).

The three-dimensional chemical, crystallographic and magnetic architecture of the cloudy zone has recently been studied using a combination of synchrotron Mössbauer spectroscopy (SMS), scanning transmission electron microscopy (STEM) tomography, atom probe tomography (APT), scanning precession electron diffraction (SPED) and micromagnetic simulations (Blukis et al. 2017; Einsle et al. 2018). The cloudy zone consists of  $\sim 10\text{-}150\ \text{nm}$  diameter islands of ferromagnetic tetrataenite embedded in a paramagnetic matrix of antitaenite, a metastable face-centered cubic (fcc) iron-nickel alloy containing  $\sim 15\text{-}25\%$  Ni. Above  $320\ \text{°C}$ , the FeNi islands adopt a disordered fcc structure (taenite). Taenite is a soft ferromagnet with low magnetocrystalline anisotropy, so that above  $320\ \text{°C}$  the islands are predicted to adopt single-vortex (SV) states. Below  $320\ \text{°C}$ , Fe and Ni atoms order onto alternating (002) layers of the parent fcc structure, yielding the tetragonal tetrataenite structure (space group  $P4/mmm$ ). The transition to tetrataenite causes the SV state to transform to an SD state on account of its high uniaxial magnetocrystalline anisotropy ( $1.37 \times 10^7\ \text{erg/cm}^3$ ). The transition from SV to SD occurs via a transient two-domain (2D) state (Einsle et al. 2018). The uniaxial easy axis of tetrataenite corresponds to the tetragonal  $c$  axis, normal to the Fe-Ni layering, which in turn corresponds to one of the three  $\langle 100 \rangle$  cubic directions of the parent taenite. The magnetic switching field of tetrataenite is predicted to be very high and has been estimated to be close to 2 T (Néel et al. 1964). Magnetic properties of tetrataenite, as measured experimentally in meteorite and artificial samples (Néel et al. 1964; Bryson et al. 2014a; Gattacceca et al. 2014), indicate the magnetic

structure in the cloudy zone is highly stable with respect to remagnetization and therefore a very useful material for paleomagnetic studies.

Although the magnetic structure of the cloudy zone is very stable, it is not easy to interpret. In their SV state above 320 °C, taenite islands are weakly to moderately interacting (Einsle et al. 2018). In their SD state below 320 °C, the tetrataenite islands are expected to interact more strongly. Quantifying interactions is important to reconstruct accurate and reliable absolute paleointensity data. Current methods used to estimate paleointensity from measurements of cloudy-zone magnetization (Maurel et al. 2019) do not account for interactions. Although such methods are sufficient to determine the presence or absence of a magnetizing field, and to provide a relative comparison of paleointensities between samples with different cooling rates, absolute paleointensities will possibly be inaccurate. Methods to simulate the remanence acquired by interacting SD particles have been developed and successfully applied to meteorites (Muxworthy et al. 2011; Muxworthy 2013; Shah et al. 2017). These methods use first-order reversal curve (FORC) diagrams to characterize the interactions between particles. However, since the cloudy zone forms a volumetrically very small part of the metal in meteorites, using FORCs to characterize the intra-cloudy zone interactions is not straightforward. The magnetic signal from the cloudy zone is very hard to separate from much stronger signals of kamacite and plessite. FORC diagrams of tetrataenite-bearing meteoritic metal show complex patterns that are poorly understood and strongly affected by interactions between the kamacite, plessite and cloudy zone components of the metal. For these reasons, a spatially resolved, high-field magnetic imaging method is desirable, as it enables the magnetic interactions between particles in the cloudy zone to be determined directly via the horizontal shift of the hysteresis loops.

## 1.2 X-ray holography

X-ray holography is well suited for examination of the cloudy zone as it can image sample magnetization with a spatial resolution of ~20–40 nm, sufficiently high to resolve individual tetrataenite islands (Eisebitt et al. 2004). Methods previously used to examine magnetic particles in geological samples, such as electron holography, magneto-optical Kerr microscopy and magnetic force microscopy, image magnetic induction or stray fields (Sarid 1994; Faigel and Tegze 1999; Qiu and Bader 2000). Inverting magnetic induction or stray fields to yield the underlying magnetization is difficult and often non-unique. Images also cannot be obtained during application of magnetic fields stronger than few tens of mT, which means only remanence states can be imaged. X-rays image magnetization directly by exploiting the X-ray magnetic circular dichroism (XMCD) effect and are not affected by stray fields. There are other methods, such as X-ray photoemission electron microscopy (XPEEM) that can achieve similar spatial resolution. However, as this method is based on imaging electrons emitted from the sample surface, imaging cannot be performed under application of strong magnetic fields. While other X-ray microscopy methods such as X-ray transmission microscopy (TXM) and scanning transmission X-ray microscopy (STXM) achieve a similar resolution to X-ray holography, the latter method is inherently unaffected by mechanical drifts as the X-ray optics and the sample are monolithically interfaced to each other. The lack of image drift allows to precisely track the magnetization of nanometer-scale particles within the hysteresis. Overall this makes X-ray holography very applicable in practice for sample examination under strong magnetic fields. X-ray holography has not been previously applied to study magnetic properties of any geological

sample. However, its capabilities have been successfully demonstrated on various artificial materials such as patterned and continuous magnetic thin films as well as magnetically capped nanospheres (Eisebitt et al. 2004; Hellwig et al. 2006; Günther et al. 2010; Pfau et al. 2014; Büttner et al. 2017). In particular, X-ray holography was used to reveal the stray-field interaction in ordered arrays of nanometer-sized magnetic islands (Pfau et al. 2014).

The principle of mask-based X-ray holography is to prepare the sample and the beam-splitting holography optics on the same x-ray transparent membrane substrate (Pfau and Eisebitt 2015). The sample is mounted on the backside of the membrane and has to be thin enough to be investigated in transmission geometry (typically thinner than 100 nm). The membrane's front side is coated with Au making it X-ray opaque. The holography optics comprises two apertures in the Au film. A micrometer-sized (1–5  $\mu\text{m}$  in diameter), typically circular, aperture is milled through the Au coating while leaving the sample intact defines the sample field of view. Adjacent to this, a small 30–50 nm aperture, so-called reference hole (or holes), is milled through both the Au coating and the sample. This hole acts as the source for the reference wave needed for holography. The combined sample object, consisting of sample aperture and reference hole(s), is exposed to a coherent beam of X-rays. The waves transmitted through the apertures interfere to produce a far-field diffraction pattern (X-ray hologram) that is recorded on a 2D detector placed downstream of the sample. The digital inverse Fourier transformation (IFT) of this x-ray hologram yields the auto-correlation of the combined sample object, consisting of a central sample-sample auto-correlation and of-centre images of sample-reference cross-correlations. Therefore each sample-reference cross-correlation contains an image of the sample that is blurred by the reference hole, such that the spatial resolution of the image is similar to the diameter of the reference hole used. The final image of a sample is produced by cropping the sample-reference cross-correlation from the IFT image and can be used for further analysis. As the sample aperture and reference hole are fixed relative to each other, the position of the reconstructed image is not affected by drift of the sample assembly, making the alignment of the resulting images very accurate (Büttner et al. 2015). To obtain magnetic contrast in the images, X-ray holograms are recorded using left- and right-circularly polarized X-rays at resonance with a suitable absorption resonance, and the difference is used to calculate the XMCD signal. The theory of the method in detail has been described elsewhere (Stroke 1965; Winthorp and Worthing 1965; Eisebitt et al. 2004).

## **2 Materials and Methods**

### **2.1 Sample description and preparation for X-ray holography**

A small sample of Tazewell IIICD iron meteorite (sample No. 16269) was provided by the Sedgwick museum of Earth Sciences, University of Cambridge, UK. This sample was selected as it shows a typical cloudy zone with medium to large maximum average island size of 92 nm (Yang et al. 1997). The meteorite and the sample were also considered to be well understood due to multiple previous studies (Scott 1973; Yang et al. 1997; Bryson et al. 2014a, 2017; Blukis et al. 2017; Einsle et al. 2018). X-ray holography sample preparation requires placing a soft X-ray transparent lamella of the meteorite onto an X-ray holography sample holder. The sample holder consisted of a silicon chip with 200 nm thick silicon nitride ( $\text{Si}_3\text{N}_4$ ) membrane windows used as substrate for X-ray imaging. The entire sample holder was coated with a multilayer consisting of 20 repeats of Cr (5 nm)/Au (55 nm) fabricated by thermal evaporation. At this thickness, the

multilayer is opaque to soft X-rays at the iron L<sub>3</sub>-absorption edge. A multilayer coating was chosen as it ensures better sputtering homogeneity during FIB milling of the aperture. A circular aperture with diameter of 5.3 μm was milled in the gold layer on top of the membrane window. Reference holes with a diameter of 40-80 nm were milled next to the aperture through the gold and Si<sub>3</sub>N<sub>4</sub> membrane. For aperture milling, a FEI HELIOS 600 Nanolab (ZELMI, TU Berlin) has been used.

To prepare the lamella the meteorite sample surface was mechanically polished using diamond suspensions with the final diamond particle size of 0.25 μm. A lamella of the cloudy zone was prepared using FEI Helios Nanolab Dual Beam focused-ion beam (FIB) and scanning electron microscope (SEM) of the Department of Material Science and Metallurgy, University of Cambridge, UK using standard techniques (Schaffer et al. 2012). The lamella was polished using the ion beam to a thickness of 50-100 nm using a procedure by (Schaffer et al. 2012). The lamella was then welded using ion-beam platinum deposition to the Si<sub>3</sub>N<sub>4</sub> membrane on top of an aperture on the other side (inset Fig. 1).

## 2.2 X-ray holography experiment

X-ray holography was performed at the UE52-SGM undulator beamline of the BESSY II synchrotron-radiation facility in Berlin, Germany. The sample was illuminated with circularly polarized soft X-rays tuned to the Fe L<sub>3</sub> absorption edge at 707 eV (1.75 nm wavelength). The silicon nitride sample holder was mounted on a larger Al holder and lowered into a high-vacuum chamber. The far-field diffraction pattern was recorded by a CCD detector (Greateyes, 2048×2048 pixels, 13.5 μm pixel size) situated 31.5 cm behind the sample. A beamstop was used to protect the detector from the intense central peak of transmitted and forward-scattered X-rays. The external magnetic field was applied using an electromagnet with four poles arranged in four quadrants around the sample. By changing magnetization at each pole, the magnetic field could be applied in-plane or out-of-plane relative to the sample surface. The maximum field strength achievable with the electromagnets used was ~1.05 T.

Two hysteresis measurements were made, with the magnetic field applied out-of-plane and in-plane relative to the sample surface. In each hysteresis loop 32 images of magnetization were taken with an average spacing between the applied field steps of ~0.1 T. Acquisition of each image required two holograms recorded at opposite beam helicities (an example hologram can be found in the supplementary information). The raw images were processed to obtain the final images of magnetization at each field step. The processing involved first removing artifacts caused by cosmic rays and background radiation that appear as very high intensity signals on individual pixels scattered randomly through the detector. After that, saturated areas, edges of the beamstop and supporting wires were smoothly masked. A high-pass filter was then applied to remove noise and the raw hologram was then centered. The difference between the holograms for left- and right-polarised light was then calculated to extract XMCD information. A real-space image is then obtained via a 2D inverse Fourier transformation. Propagation of the reconstructed complex image (reflecting both amplitude and phase information) to the plane where the reference beam has the smallest waist was performed, in order to enhance the spatial resolution of the reconstructed image. This was followed by phase ramp compensation to suppress artifacts

due to sample thickness change over the field of view. A cross-correlation containing the magnetic image of the sample was then cropped out and used for analysis. The phase was then rotated to obtain maximum magnetic contrast in the real part of the reconstruction. For visualization only, the image was linearly interpolated to four times larger size.

### 2.3 Simulations using FORCulator

FORC diagrams of an interacting ensemble of SD tetrataenite islands were simulated using the FORCulator code (Harrison and Lascu 2014). The cloudy zone was modeled as an assemblage of 100 spherical particles, each 70 nm in diameter, randomly dispersed in a cubic box with packing fraction 50%. This corresponds approximately to the center of the experimentally measured region. Each particle was given a random coercivity picked from the distribution of coercivities observed experimentally in the X-ray holography out-of-plane dataset. Easy axes were assigned randomly to the three possible  $\langle 100 \rangle$  directions. Each simulation contained 100 individual FORCs with a field step size of 0.0025 mT. The conversion from individual FORCs to the final FORC diagram was performed according to the methodology described in (Harrison and Lascu 2014). The results presented represent the average of 100 separate simulations, each generated with a random placement of particles and new random assignment of coercivities from the distribution observed in X-ray holography.

## 3 Results

### 3.1 X-ray holography

In total, 32 magnetization images were obtained in both in-plane and out-of-plane hysteresis loops (see Fig. 2 for a representative example of a single image and Fig 3. for a selected image sequence). The magnetic field was changed from  $\sim -1$  T to  $\sim 1$  T back to  $\sim -1$  T. The images within hysteresis series are inherently aligned to each other in terms of translational image drift. Only sample rotation had to be corrected, however, this was negligible in almost all images. Full sequence of magnetic images from both hysteresis loops are attached to supplemental information as mp4 files. Each pixel represents sample magnetization at that specific location throughout the magnetic field images. Hence, a hysteresis loop of each pixel can be extracted. The pixel size in the magnetization images was  $20 \text{ nm} \times 20 \text{ nm}$ . Hysteresis loops were observed to often change very rapidly in appearance from one pixel to the next, therefore the spatial resolution was inferred to be diffraction limited to 40 nm. The hysteresis loops of the tetrataenite islands are expected to show square hysteresis behavior, with islands switching between two magnetization states (Fig. 4). Although many pixels did show this behavior, a significant number of pixels showed complex or distorted hysteresis loops. This was considered to occur due to overlapping islands and a large matrix contribution to the signal. Some unusual, such as reversed, hysteresis loops were also observed and were excluded from analysis as they arise as a consequence of using a beamstop in the experiment. The beamstop blocks the central peak of the far-field diffraction pattern and effectively acts as a high-pass filter removing spatially slow variations in the magnetization. This means the island magnetization measured is relative to the immediate surroundings and can lead to apparent reverse hysteresis loops in the case of low-magnitude magnetization. This artifact has been simulated and demonstrated not to affect the results elsewhere (Blukis 2018). Each pixel was examined manually and only pixels that showed

clear two-state hysteresis behavior with noise level such that up and down domain magnetization values did not overlap were selected for analysis. Pixels with very noisy, unusual, complex or reversed hysteresis loops were not analyzed further.

To analyze the individual hysteresis loops, a folded square wave was fitted to the measured loop using least-squares fitting (Fig. 4). The square wave is defined by two critical switching fields,  $B_a$  and  $B_b$ , which correspond to the fields needed to switch from the upper to the lower branch and from the lower to the upper branch of the hysteresis loop, respectively.

The coercivity  $B_c = -(B_b - B_a)/2$  and horizontal offset  $B_u = (B_b + B_a)/2$  values were then calculated from these fitted loops. According to conventional Preisach interpretation, the horizontal offset is equated with the interaction field acting on the island. Average  $B_c$  and  $B_u$  values, as well as distributions (Fig. 5) were calculated from the individual pixel data. In total 885 pixels were analyzed in the out-of-plane and 2108 pixels in the in-plane hysteresis datasets. Analysis was performed on individual pixels rather than islands that could have been obtained by averaging neighboring pixels with similar hysteresis properties. The pixels were analyzed individually as the pixel assignment to a particular island was often ambiguous as neighboring pixels often showed noticeably different hysteresis properties, this was particularly noticeable in the in-plane dataset. The distribution of analyzed pixels was random throughout the cloudy zone (see Fig. 6a) in the out-of-plane dataset. In the in-plane dataset the analyzed pixel density was higher in the coarse cloudy zone (see Fig. 6b), however, the pixel assignment was ambiguous. As there was also a systematic coercivity change with island size the coercivity distribution of pixels may be slightly more shifted to low coercivity values as compared to one that would be obtained from island coercivities. However, this is expected to be only a slight change and would not affect the interpretation of the results or conclusions. The offset distributions are unaffected by this as offset values varied at random with respect to position or island size in both datasets.

The average coercivity of the tetraenaite islands was calculated to be 0.5 T in the out-of-plane dataset and 0.4 T in the in-plane dataset. However, the coercivity showed a wider distribution in the out-of-plane dataset, therefore a single average value is not a good approximation of the sample (Fig. 5a). Some islands in the out-of-plane dataset had coercivities in excess of 0.8 T. The offset shows maximum value near zero field in histograms of both datasets, and although the in-plane dataset shows an average value towards slightly negative values, this is within error of zero. The errors in coercivity and offset are estimated 0.05 T, and were determined by the average field step which was  $\sim 0.1$  T. Offset distributions in both experiments are not consistent with simple Gaussian or Lorentzian distributions (Fig. 5b).

The coercivity and offset data allows for Preisach diagrams to be generated (see Fig. 5c,d). These diagrams show similar information to a FORC diagram especially in a system consisting of single-domain particles.

The spatial distribution of coercivities for out-of-plane and in-plane fields is shown in Fig. 6a,b. There is no apparent spatial distribution order of island coercivities in the out-of-plane dataset, even though island size does systematically decrease as the distance from tetraenaite rim increase (Fig. 6c). In contrast, there is a clear increase in the coercivity values with decreasing cloudy-zone island size for the in-plane dataset. Offset values in both datasets had a random

spatial distribution. Islands were observed to have significantly different coercivities depending on the measurement geometry (see Fig. 6d).

### 3.2 FORCulator results and comparison with the experiment

Simulations using FORCulator using the experimentally measured coercivity distributions from the out-of-plane dataset produced similar offset distributions to those observed using X-ray holography, however, the distribution was narrower and more similar to that observed in the in-plane dataset.

Fig. 8 shows four different offset distributions, three experimental and one simulated using FORCulator (Harrison and Lascu 2014). The offset distributions of FORC diagrams were obtained by projecting the FORC diagrams onto the  $B_u$  axis. However, as FORC distributions and Preisach distributions are in general not equivalent, there are features in the experimental FORC distribution that need to be understood before this projection can be interpreted as an offset distribution. The sample of Marjalahti pallasite contains not only the cloudy zone but also phases like plessite. Due to experimental constraints the FORC diagram does not extend further than 0.18 T on the  $H_u$  axis. The central feature in the FORC diagram did, within experimental error, match the broadness of the offset distribution observed in the X-ray holography experiment. The peak in the offset distribution is located similar distance away from zero as the offset distributions measured in X-ray holography. The in-plane and out-of-plane datasets demonstrate different offset peak broadness and shape. The experimental FORC is approximately in between the two in terms of its offset distribution and probably represents the effect of orientation averaging in the experimental FORC measurement. The major difference between in-plane and out-of-plane datasets is the much narrower offset distribution in the in-plane dataset. If the offset from zero by about 0.05 T in the X-ray holography offsets is ignored, the simulated offset distribution using FORCulator is also a close match to the measured offset distribution in the in-plane dataset. The offset from zero could be caused by a coarse field sampling step of  $\sim 0.1$  T that was used in the X-ray holography experiment. Finer sampling would more accurately describe the hysteresis loops and therefore more accurate coercivity and offset values. This is more important for offsets as the magnitudes of offset values are significantly smaller than the coercivity values and are therefore more susceptible to such errors.

## 4 Discussion

The coercivity distribution of the out-of-plane sample (Fig. 5a) shows that while any coercivity value up to  $\sim 1$  T (maximal possible coercivity to be measured with this experimental setup), there are peaks in the histogram at 0.2 T and 0.7 T. This is most likely due to the limited easy axis directions of tetrataenite in the cloudy zone. Tetrataenite islands can have the tetragonal axis only along  $\langle 100 \rangle$  directions of the parent face-centered-cubic (fcc) as tetrataenite forms by chemical ordering of Fe and Ni atoms while maintaining the overall face-centered-cubic superstructure. In our case it was found by electron backscatter diffraction that the sample consists of a single fcc crystal and the  $\langle 100 \rangle$  directions form angles of  $\sim 73$ ,  $57$  and  $37$  degrees to the applied field direction (normal to sample surface) (see supplemental information). The significantly different angles between the easy axes of tetrataenite and the applied field are likely to be the cause of certain coercivity values being more likely than others. In the Preisach diagram

(see Fig. 5c) three higher intensity regions can be seen that possibly are caused by the three different sets of easy axes. However, this is not the only factor affecting the observed coercivity as all coercivity values between  $\sim 0$  T and  $\sim 1$  T were observed. No such effects have been observed in the in-plane dataset. The in-plane dataset is heavily influenced by the presence of ferromagnetic matrix that appears in thin lamellae samples due to electronic ground state change from low moment ferrimagnetic to high moment ferromagnetic state and therefore could be considered less representative of unaltered bulk cloudy zone that contains paramagnetic matrix. The effect of ferromagnetic matrix as well as that of artificially altered particle geometries in a lamella was explored by micromagnetic simulations and is reported in the supplemental information.

While it is theoretically possible that the coercivity difference between the two datasets (see Figs. 5a, 6d) is caused by majority of islands having easy axis such that lower coercivities are observed in the in plane dataset, this is considered highly unlikely as island easy axis distributions in an area of cloudy zone as large as the one studied are expected to be nearly equal based on observations from other studies (Bryson et al. 2014b, 2014a; Einsle et al. 2018). Biased easy axis distribution would also not explain why in the in-plane dataset a systematic, island size-dependent variation in coercivity is observed while it is absent in the out-of-plane dataset. As the simulations using FORCulator do not account for the impact of the ferromagnetic matrix, they are more representative of a bulk cloudy zone. FORC diagrams of meteoritic metal, such as one obtained from Marjalahti pallasite (Nichols et al. 2016) commonly show a weak broad diffuse ridge. The ridge is similar to what is normally associated with single domain particles but is a lot broader. Based on the Preisach distributions obtained in this work it appears this diffuse ridge is caused by the cloudy zone. The offset values observed in the FORC diagram of the bulk meteorite (Marjalahti pallasite) sample (see Fig. 8) are slightly wider than those calculated using FORCulator or the in-plane dataset, however, are narrower than those observed in the out-of-plane dataset. The two X-ray holography datasets show very different offset distributions and while, due to the effects of ferromagnetic matrix, in-plane dataset could be disregarded as non-representative, it is also likely that the out-of-plane dataset represents the opposite extreme. Despite this out-of-plane dataset is considered to be more representative as the influence of the artificially induced magnetization of the matrix is minimized. By using the coercivities observed in the out-of-plane dataset FORCulator has produced offset distribution that is narrower than the one observed using X-ray holography. This indicates the interaction field experienced by the islands in the actual cloudy zone is higher than that simulated. As the magnetic properties used have been experimentally observed in tetraenaite the most likely source of discrepancy is the description of the cloudy zone as randomly positioned spherical particles with a packing fraction of 50% that might not be being entirely representative of the real cloudy zone. In cloudy zone both the packing fraction and the island shape will be different. This has been observed using electron tomography (Einsle et al. 2018) and shows the islands may have elongated, bent and partially matching or interlocking shapes that would increase one islands exposure to the magnetic field produced by another. This would result in significantly higher interaction field. Nevertheless, simulations using FORCulator demonstrate that magnetostatic interactions are significant in systems like the cloudy zone and can be simulated to relatively high degree. Provided appropriate particle geometries and packing fractions could be provided, for example, by performing a simulated spinodal decomposition, the FORC diagram calculated is very likely to be consistent with observations made using X-ray holography.

## 4 Conclusions

By performing this experiment, we have directly measured in-field hysteresis behavior under high applied field of individual paleomagnetic remanence carriers in a meteoritic cloudy zone. We have also confirmed the cloudy zone to be an assemblage of interacting single-domain particles at room temperature. This explains the diffuse high-coercivity signal in FORC diagrams of bulk samples. Tetrataenite islands demonstrate two-state single-domain behavior. Most of the individual islands show high coercivities implying high stability. This confirms a stable remanence can be carried by the cloudy zone. However, it was also shown by this experiment that to model remanence acquisition by the cloudy zone, models that consider interactions should be used. The only studies that have included magnetostatic interactions between particles (Shcherbakov et al. 1995; Shcherbakov and Sycheva 1996; Muxworthy et al. 2011), so far have modelled only weakly interacting samples with the magnetic particle mass fraction of few %. Also, the final magnetization state is assumed to be acquired as the particles cool through the blocking temperature without significant change of material magnetic properties. This is a significant difference from the cloudy zone, where the packing fraction of the magnetic tetrataenite islands is ~20-60 % by volume. Furthermore, it has been shown that the cloudy zone acquires magnetization during the chemical ordering transition of magnetic taenite islands into tetrataenite (Einsle et al. 2018). During this process, magnetic remanence of the nearly isotropic taenite islands is converted into magnetic remanence of the highly uniaxial tetrataenite islands by steadily changing magnetocrystalline anisotropy from cubic to highly uniaxial. Considering the very significant change and new constraints on the allowable magnetization directions in the new assembly of tetrataenite (formerly taenite) it is inevitable that the new magnetic remanence is highly altered. This process has been qualitatively explored before (Einsle et al. 2018), however, more detailed work and quantitative modelling is required to fully understand the process and reconstruct quantitative paleointensity data. Although a complicated task, the ultimate reconstruction of quantitative paleointensities from meteoritic cloudy zone would enable more accurate and complete insight into planetary body and system evolution processes.

This experiment demonstrates the feasibility of applying X-ray holography to directly image magnetization of natural samples with a spatial resolution of 40 nm. Furthermore, such imaging can be performed under high applied fields, therefore, in-field behavior of paleomagnetic remanence carriers can be directly studied. The method avoids the drawbacks of other nanoscale magnetic imaging methods such as electron holography or magnetic force microscopy by using an imaging probe that allows magnetization to be directly imaged. This is also an improvement over other X-ray methods such as X-ray photoemission electron microscopy and transmission X-ray microscopy, as there is very little image drift as a function of applied field, making the extraction of high-resolution hysteresis loops on a pixel-by-pixel basis more reliable. It could be used in the future to examine materials like magnetite-ulvöspinel or titanomagnetite-titanohematite intergrowths, as these also show complicated nanoscale magnetization patterns. Magnetic in-field behavior of other naturally occurring particles such as vortex state particles or particle chains could also be examined.

## Acknowledgments

This work was supported by the European Research Council under the European Union's Seventh Framework Programme (FP/2007-2013)/ ERC grant agreement numbers 320750 and 312284. We thank the Sedgwick Museum, University of Cambridge for the sample of Tazewell meteorite. The authors declare no conflict of interest. Data used in this study is available at ([zenodo.org/record/3709017](https://zenodo.org/record/3709017)).

## References

- Bai, X.N., and Stone, J.M. (2013) Local study of accretion disks with a strong vertical magnetic field: Magnetorotational instability and disk outflow. *Astrophysical Journal*, 767, 1–18.
- Blukis, R. (2018) A combined experimental and computational study of nanopaleomagnetic recorders in meteoritic metal. University of Cambridge.
- Blukis, R., Rüffer, R., Chumakov, A.I., and Harrison, R.J. (2017) A high spatial resolution synchrotron Mössbauer study of the Tazewell III CD and Esquel pallasite meteorites. *Meteoritics & Planetary Science*, 52, 925–936.
- Bryson, J.F.J., Church, N.S., Kasama, T., and Harrison, R.J. (2014a) Nanomagnetic intergrowths in Fe–Ni meteoritic metal: The potential for time-resolved records of planetesimal dynamo fields. *Earth and Planetary Science Letters*, 388, 237–248.
- Bryson, J.F.J., Herrero-Albillos, J., Kronast, F., Ghidini, M., Redfern, S. a. T., van der Laan, G., and Harrison, R.J. (2014b) Nanopaleomagnetism of meteoritic Fe–Ni studied using X-ray photoemission electron microscopy. *Earth and Planetary Science Letters*, 396, 125–133.
- Bryson, J.F.J., Nichols, C.I.O., Herrero-Albillos, J., Kronast, F., Kasama, T., Alimadadi, H., van der Laan, G., Nimmo, F., and Harrison, R.J. (2015) Long-lived magnetism from solidification-driven convection on the pallasite parent body. *Nature*, 517, 472–475.
- Bryson, J.F.J., Weiss, B.P., Harrison, R.J., Herrero-Albillos, J., and Kronast, F. (2017) Paleomagnetic evidence for dynamo activity driven by inward crystallisation of a metallic asteroid. *Earth and Planetary Science Letters*, 472, 152–163.
- Büttner, F., Moutafis, C., Schneider, M., Krüger, B., Günther, C.M., Geilhuffe, J., Schmising, C. V, Mohanty, J., Pfau, B., Schaffert, S., and others (2015) Dynamics and inertia of skyrmionic spin structures. *Nature Physics*, 11.
- Büttner, F., Lemesh, I., Schneider, M., Pfau, B., Günther, C.M., Hessing, P., Geilhuffe, J., Caretta, L., Engel, D., Krüger, B., and others (2017) Field-free deterministic ultra-fast creation of magnetic skyrmions by spin-orbit torques. *Nature Nanotechnology*, 12.
- Einsle, J.F., Eggeman, A.S., Martineau, B.H., Saghi, Z., Collins, S.M., Blukis, R., Bagot, P.A.J., Midgley, P.A., and Harrison, R.J. (2018) Nanomagnetic properties of the meteorite cloudy zone. *Proceedings of the National Academy of Sciences*, 115.
- Eisebitt, S., Lüning, J., Schlotter, W.F., Hellwig, O., Eberhardt, W., and Stöhr, J. (2004) Lensless imaging of magnetic nanostructures by X-ray. *Nature*, 432, 885–888.
- Faigel, G., and Tegze, M. (1999) X-ray holography. *Reports on Progress in Physics*, 62, 355–393.
- Fu, R.R., Weiss, B.P., Shuster, D.L., Gattacceca, J., Grove, T.L., Suavet, C., Lima, E. a, Li, L., and Kuan, A.T. (2012) An ancient core dynamo in asteroid Vesta. *Science (New York, N.Y.)*, 338, 238–41.

- Fu, R.R., Weiss, B.P., Lima, E.A., Harrison, R.J., Bai, X.N., Desch, S.J., Ebel, D.S., Suavet, C., Wang, H., Glenn, D., and others (2014) Solar nebula magnetic fields recorded in the Semarkona meteorite. *Science*, 346, 1089–1092.
- Gattacceca, J., Suavet, C., Rochette, P., Weiss, B.P., Winklhofer, M., Uehara, M., and Friedrich, J.M. (2014) Metal phases in ordinary chondrites: Magnetic hysteresis properties and implications for thermal history. *Meteoritics & Planetary Science*, 49, 652–676.
- Günther, C.M., Hellwig, O., Menzel, A., Pfau, B., Radu, F., Makarov, D., Albrecht, M., Goncharov, A., Schrefl, T., Schlotter, W.F., and others (2010) Microscopic reversal behavior of magnetically capped nanospheres. *Physical Review B - Condensed Matter and Materials Physics*, 81, 1–7.
- Harrison, J.R., and Lascu, I. (2014) FORCulator: A micromagnetic tool for simulating first-order reversal curves. *Geochemistry, Geophysics, Geosystems*, 4671–4691.
- Hellwig, O., Eisebitt, S., Eberhardt, W., Schlotter, W.F., Lüning, J., and Stöhr, J. (2006) Magnetic imaging with soft x-ray spectroholography. *Journal of Applied Physics*, 99, 2004–2007.
- Maurel, C., Weiss, B.P., and Bryson, J.F.J. (2019) Meteorite cloudy zone formation as a quantitative indicator of paleomagnetic field intensities and cooling rates on planetesimals. *Earth and Planetary Science Letters*, 513, 166–175.
- Muxworthy, A. (2013) The role of magnetic interactions in natural systems. *Astronomy and Geophysics*, 54, 31–35.
- Muxworthy, A.R., Heslop, D., Paterson, G.A., and Michalk, D. (2011) A Preisach method for estimating absolute paleofield intensity under the constraint of using only isothermal measurements: 2. Experimental testing. *Journal of Geophysical Research: Solid Earth*, 116, 1–20.
- Néel, L., Pauleve, J., Pauthenet, R., Laugier, J., and Dautreppe, D. (1964) Magnetic properties of an iron-nickel single crystal ordered by neutron bombardment. *Journal of Applied Physics*, 35, 873.
- Nichols, C.I.O., Bryson, J.F.J., Herrero-Albillos, J., Kronast, F., Nimmo, F., and Harrison, R.J. (2016) Pallasite paleomagnetism: Quiescence of a core dynamo. *Earth and Planetary Science Letters*, 441, 103–112.
- Pfau, B., and Eisebitt, S. (2015) *Synchrotron Light Sources and Free-Electron Lasers*. Springer.
- Pfau, B., Günther, C.M., Hauet, T., Hannen, T., Eisebitt, S., and Hellwig, O. (2014) Influence of stray fields on the switching-field distribution for bit-patterned media based on pre-patterned substrates. *Applied Physics Letters*, 105.
- Qiu, Z.Q., and Bader, S.D. (2000) Surface magneto-optic Kerr effect. *Review of Scientific Instrumentation*, 71.3, 1243–1255.
- Santos, F., Dowell, C.D., Houde, M., Looney, L., Lopez-Rodriguez, E., Novak, G., and Ward-Thompson, D. (2018) HAWC+/SOFIA observations of Rho Oph A: far-infrared polarization spectrum. In *American Astronomical Society Meeting Abstracts* p. 231.
- Sarid, D. (1994) *Scanning force microscopy: with applications to electric, magnetic and atomic forces*. Oxford University Press.
- Schaffer, M., Schaffer, B., and Ramasse, Q. (2012) Sample preparation for atomic-resolution STEM at low voltages by FIB. *Ultramicroscopy*, 114, 62–71.
- Scott, E.R.D. (1973) The nature of dark-etching rims in meteoritic taenite. *Geochimica et Cosmochimica Acta*, 37, 2283–2294.

- Shah, J., Bates, H.C., Muxworthy, A.R., Hezel, D.C., Russell, S.S., and Genge, M.J. (2017) Long-lived magnetism on chondrite parent bodies. *Earth and Planetary Science Letters*, 475, 106–118.
- Shcherbakov, V.P., and Sycheva, N.K. (1996) Monte Carlo modelling of TRM and CRM acquisition and comparison of their properties in an ensemble of interacting SD grains. *Geophysical Research Letters*, 23, 2827–2830.
- Shcherbakov, V.P., Lamash, B.E., and Sycheva, N.K. (1995) Monte-Carlo modelling of thermoremanence acquisition in interacting single-domain grains. *Physics of the Earth and Planetary Interiors*, 87, 197–211.
- Simon, J.B., Bai, X.N., Armitage, P.J., Stone, J.M., and Beckwith, K. (2013) Turbulence in the outer regions of protoplanetary disks. II. Strong accretion driven by a vertical magnetic field. *Astrophysical Journal*, 775.1, 73.
- Stroke, G.W. (1965) Lenseleff Fourier-transform method for optical holography. *Applied Physics Letters*, 6, 201–203.
- Wang, H., Weiss, B.P., Bai, X.N., Downey, B.G., Wang, Jun, Wang, Jiajun, Suavet, C., Fu, R.R., and Zucolotto, M.E. (2017) Lifetime of the solar nebula constrained by meteorite paleomagnetism. *Science*, 355, 623–627.
- Wardle, M. (2007) Magnetic fields in protoplanetary disks. *Astrophysics and Space Science*, 311, 35–45.
- Winthorp, J.T., and Worthing, C.R. (1965) X-ray microscopy by successive Fourier transformation. *Physics Letters*, 15, 124–126.
- Yang, C.W., Williams, D.B., and Goldsteini, J.I. (1997) A new empirical cooling rate indicator for meteorites based on the size of the cloudy zone of the metallic phases. *Meteoritics & Planetary Science*, 32, 423–429.

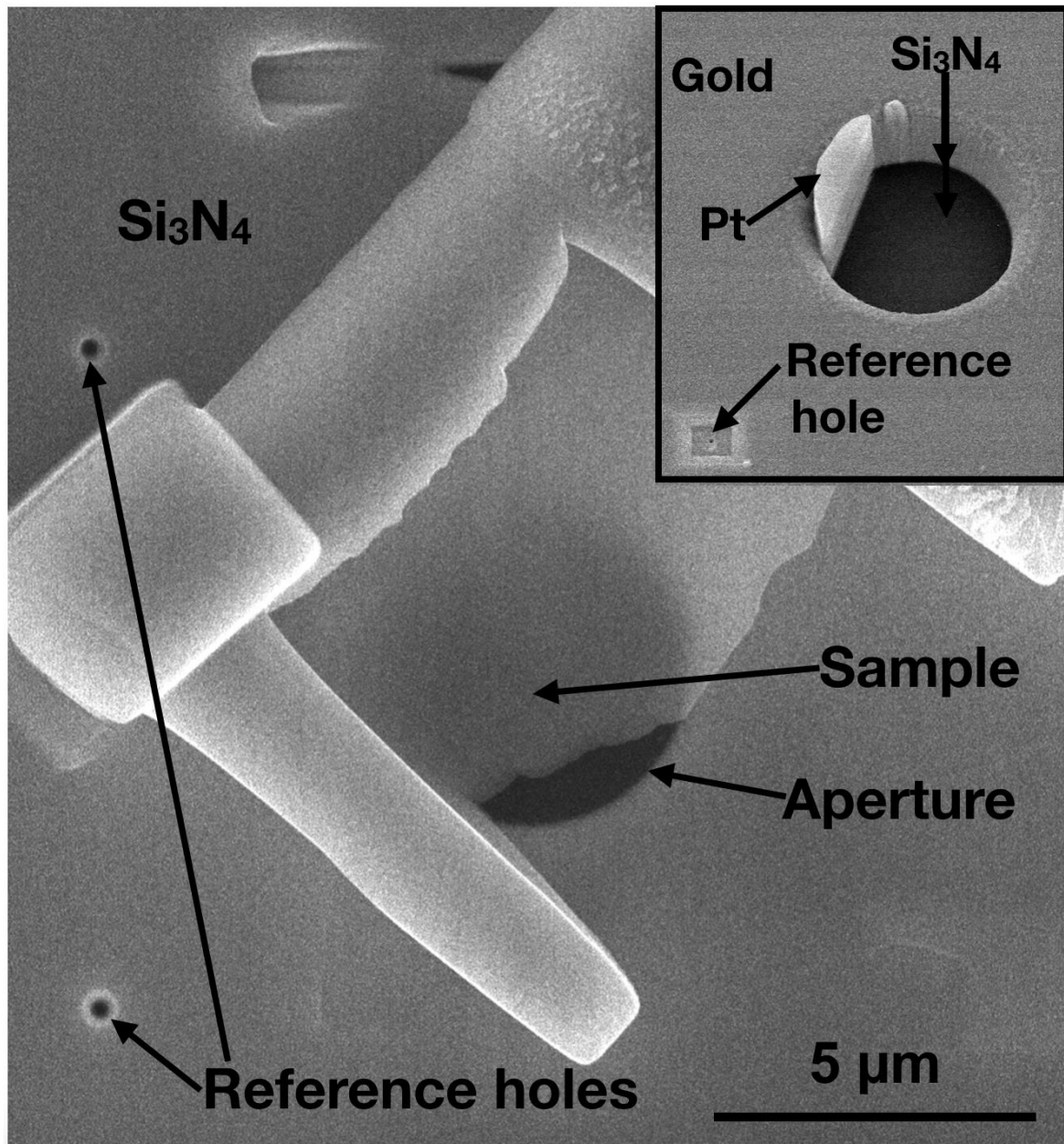


**Figure 1.** A ~60-100 nm thick lamella of the Tazewell meteorite on a silicon nitride membrane prepared for an X-ray holography experiment. The inset shows the reverse side (gold side) of the sample holder chip. The sample did not cover the entire aperture and the excess X-rays allowed through the aperture were stopped by platinum deposited on the reverse side of the sample. Only a single reference hole was used. Other holes in the Au coating were covered with platinum on the reverse side.

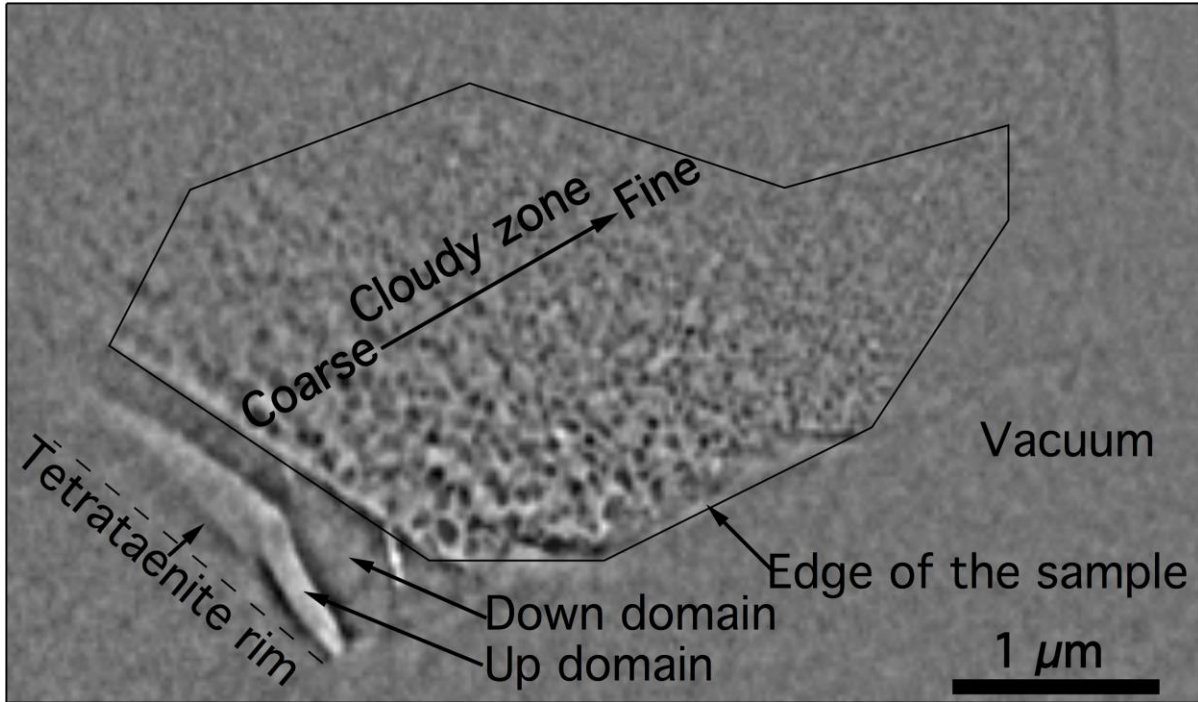


**Figure 2.** A representative image of the magnetization of the cloudy zone. White pixels indicate magnetization out of the plane of the diagram, black pixels indicate magnetization into the plane of the diagram. This image has been obtained at -0.6 T applied magnetic field in out-of-plane geometry.

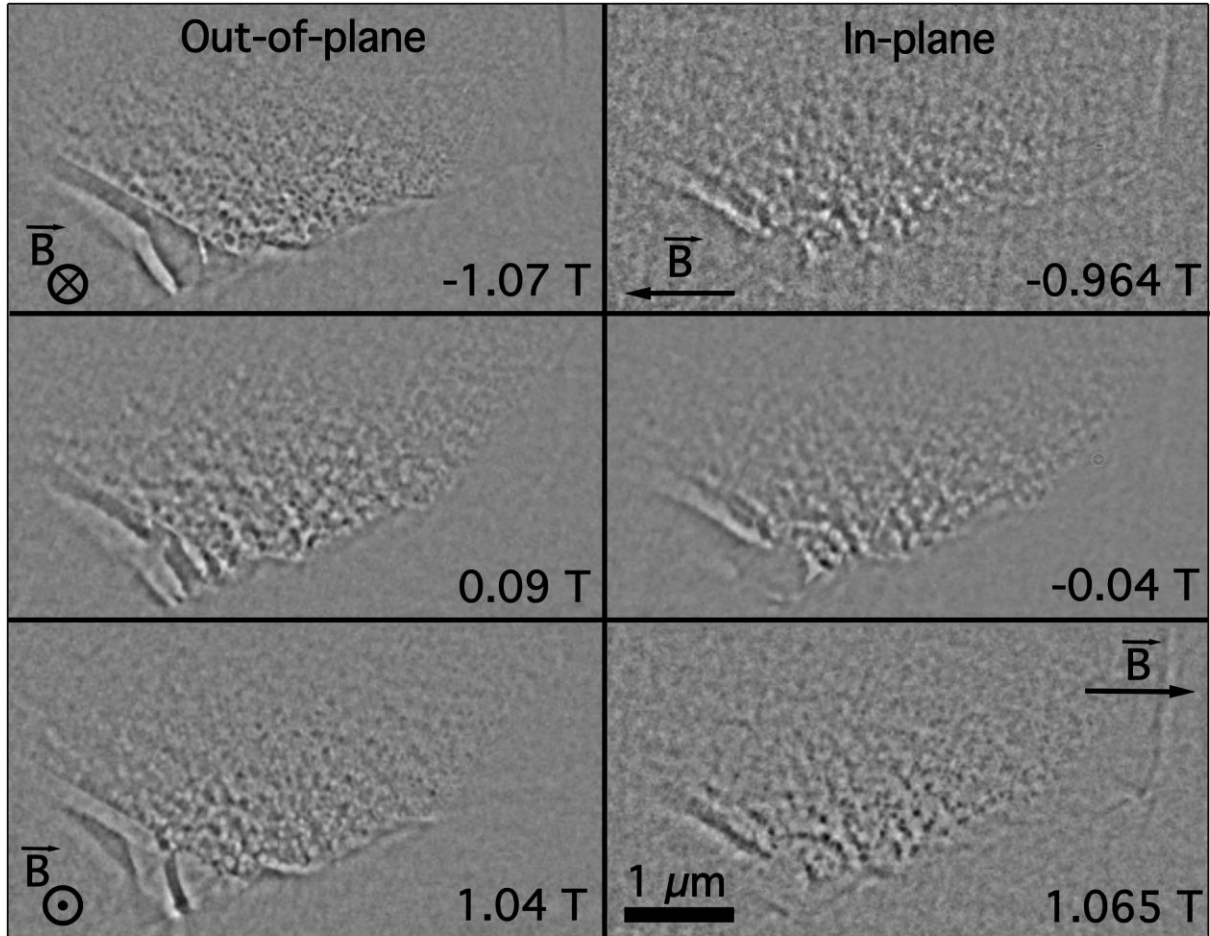


**Figure 3.** A sequence of images from the hysteresis loops with the magnetic field applied out-of-plane (left) relative and in-plane (right) to the sample surface. White pixels indicate magnetization out of the plane of the diagram (positive direction), black pixels indicate magnetization into the plane of the diagram (negative direction). During hysteresis loop acquisition the applied field was changed from negative to positive and back to negative saturation. The images at 0.09 T and -0.04 T represent the approximate remanence states after negative saturation.  $B$  indicates the applied field direction. For a full sequence of all magnetic images obtained in both hysteresis loops see supplemental information.

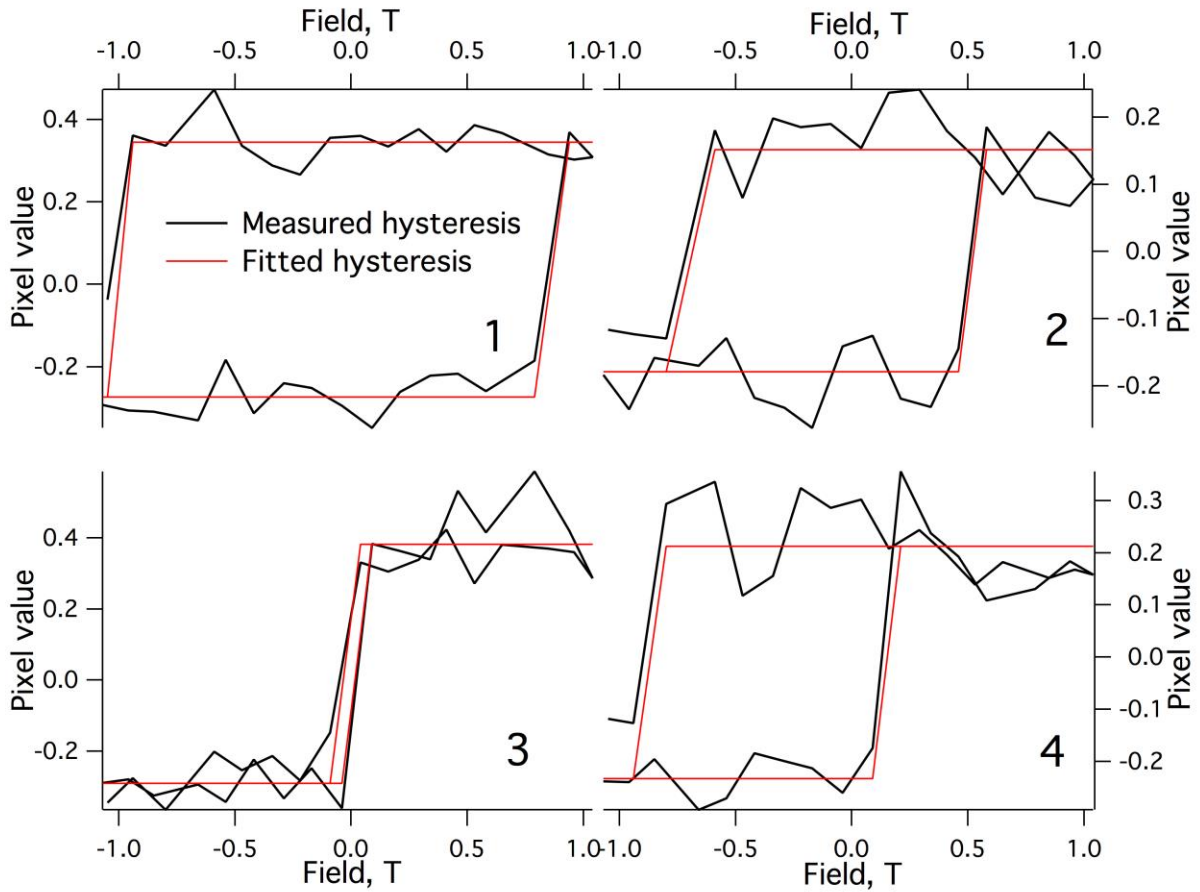


**Figure 4.** Four representative single-pixel hysteresis loops in the out-of-plane dataset. Significant variability in coercivities and offset values was observed. The loops were fitted assuming that each island is a single domain with only two allowed magnetization directions. The positions of the islands corresponding to these hysteresis loops are shown in Fig. 6a,c.

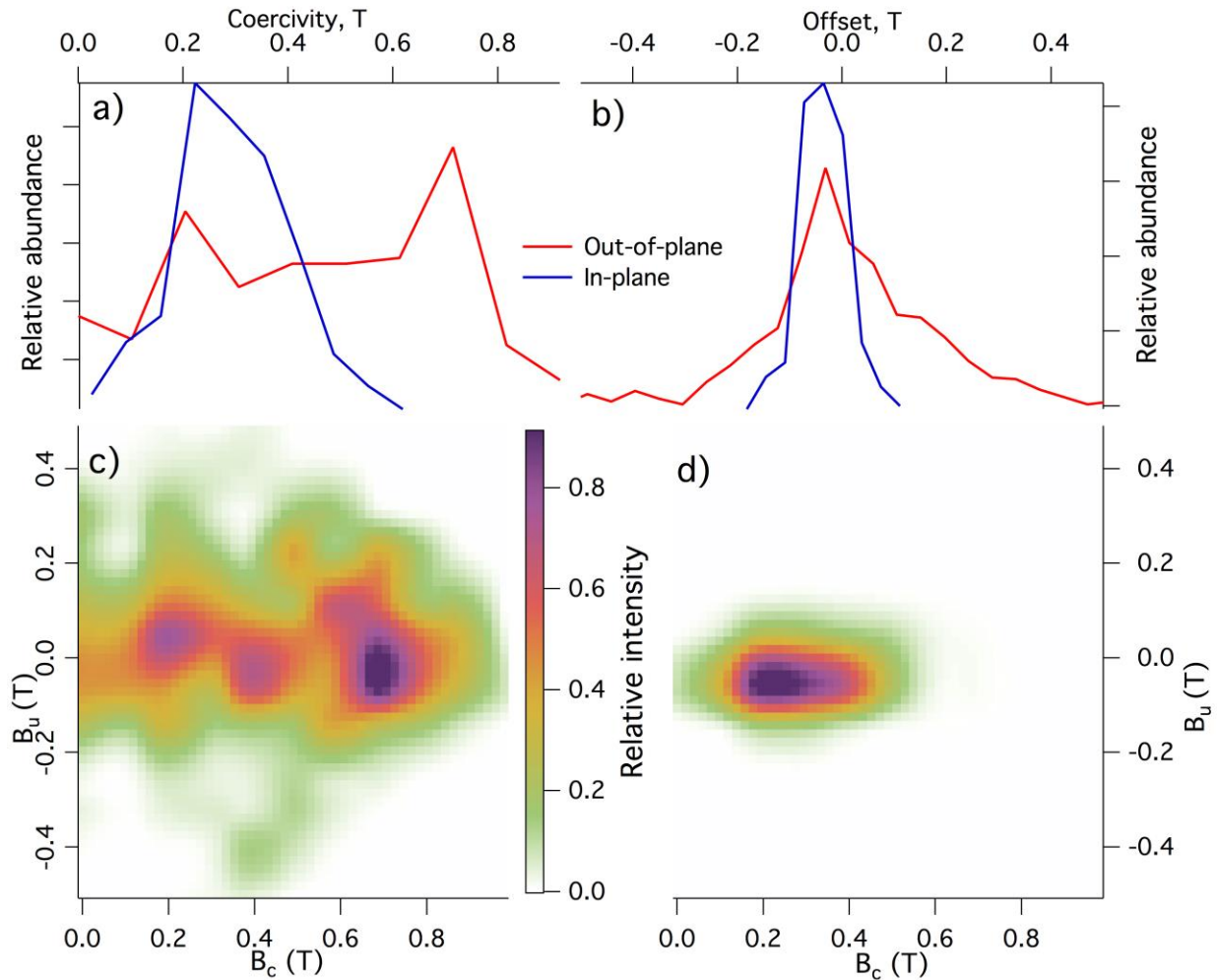


**Figure 5.** a) Histograms of coercivity ( $B_c$ ) and (b) horizontal offset ( $B_u$ ) for the out-of-plane and in-plane datasets. (c,d) Measured Preisach (FORC-like) distributions of the sample with the magnetic field being applied out-of-plane (c) and in-plane (d). Preisach diagram images have been bilinearly interpolated to five times larger size and smoothed.

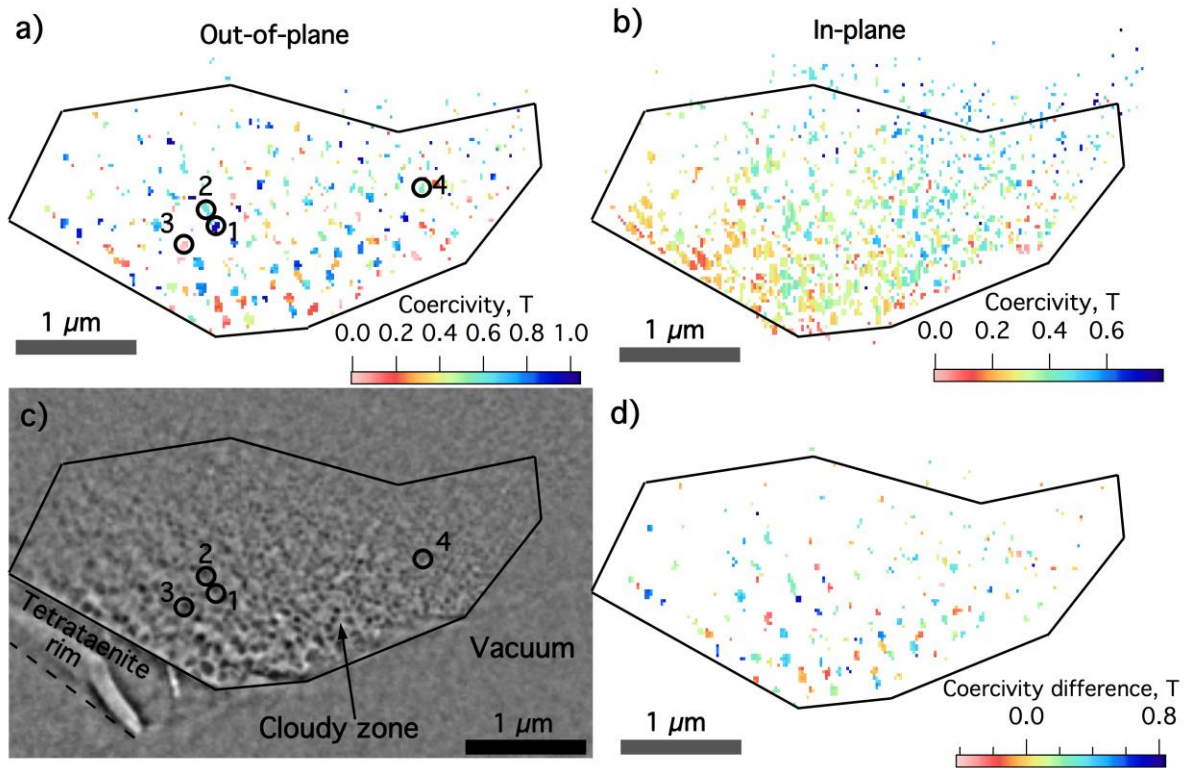


**Figure 6.** a) Map of coercivities in the out-of-plane dataset. b) Map of coercivities in the in-plane dataset. This dataset shows systematic increase in coercivity with decreasing particle size. c) Magnetic image of the sample, numbered circles indicate positions of the hysteresis loops shown in Fig. 4. d) Map of coercivity differences between the out-of-plane and in-plane datasets where good hysteresis loops could be obtained in both datasets.

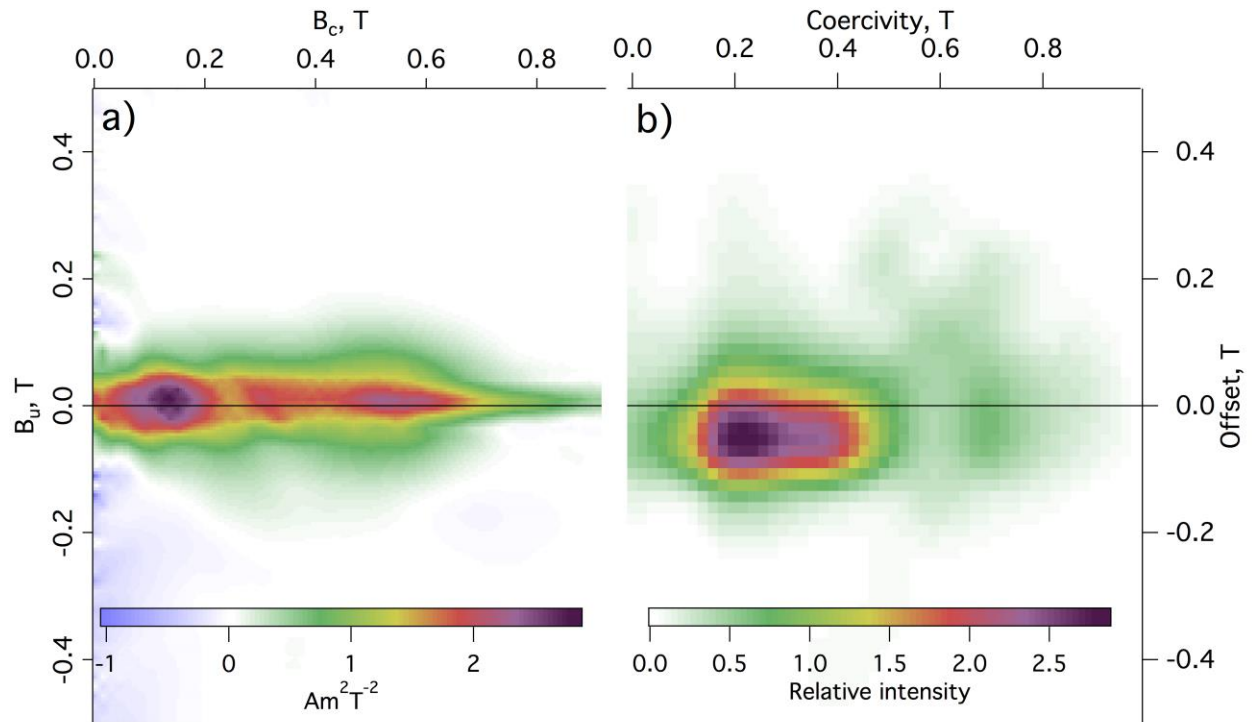


**Figure 7.** a) A simulated FORC diagram using FORCulator code. b) A combined Preisach distribution of both in-plane and out-of-plane datasets. Preisach distributions of both datasets were assigned an equal total weighting and rescaled to a comparable intensity to the FORC diagram obtained using FORCulator for comparison. The Preisach distribution b) has been interpolated to five times larger size and smoothed, processing of the FORC diagram shown in a) is described in methods.

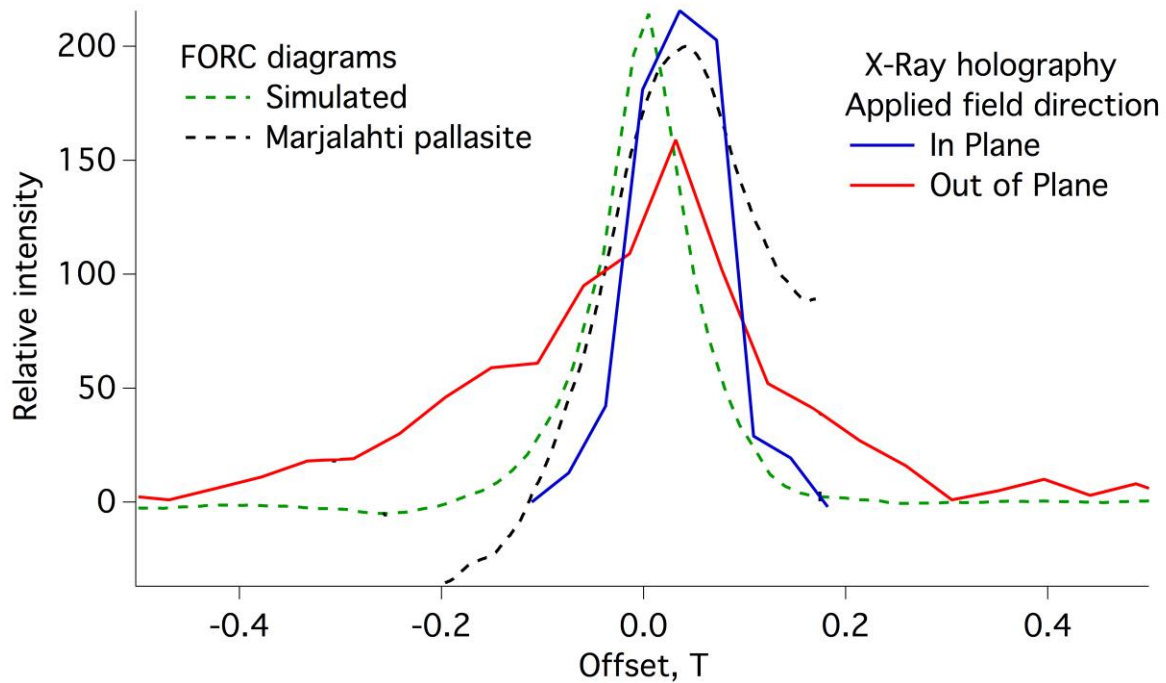


**Figure 8.** Offset distributions measured in the X-ray holography experiment (red and blue lines). Green dashed line represents the simulated offset distribution using FORCulator (extracted from FORC diagram shown in Fig. 7a). Offset distribution is also shown for an experimentally measured FORC diagram of the Marjalahti pallasite (Nichols et al. 2016). The intensities of both FORC distributions were adjusted to be comparable to the histograms extracted from X-ray holography datasets. To make comparison between offset distributions easier, the two offset distributions extracted from X-ray holography are reversed. This was considered appropriate since they are extracted from Preisach and not FORC distributions.